

Prethermal Time-Crystalline Corner Modes

Si Jiang,¹ Dong Yuan,¹ Wenjie Jiang,¹ Dong-Ling Deng,^{1,2,3,*} and Francisco Machado^{4,5,†}

¹Center for Quantum Information, IIIS, Tsinghua University, Beijing 100084, China

²Hefei National Laboratory, Hefei 230088, China

³Shanghai Qi Zhi Institute, 41st Floor, AI Tower, No. 701 Yunjin Road, Xuhui District, Shanghai 200232, China

⁴ITAMP, Harvard-Smithsonian Center for Astrophysics, Cambridge, Massachusetts 02138, USA

⁵Department of Physics, Harvard University, Cambridge, Massachusetts 02138, USA

We demonstrate the existence of prethermal discrete time crystals whose sub-harmonic response is entirely localized to zero-dimensional corner modes. Within the exponentially long prethermal regime, we show that the robustness of these corner modes arises from two related, yet distinct mechanisms: the presence of a higher-order symmetry-protected topological phase in the effective Hamiltonian, or the emergence of a dynamical constraint that prevents the decay of the corner mode. While the first mechanism ensures the stability of the sub-harmonic response throughout the entirety of the prethermal regime, it is restricted to initial states in the ground state manifold of the effective Hamiltonian. By contrast, the second mechanism enables the observation of the prethermal time-crystalline order for *arbitrary initial states*, albeit with a time scale that is not only determined by the frequency of the drive, but also the relative energy scale across the system's sublattices. We characterize these two mechanisms by simulating the dynamics of a periodically driven two-dimensional spin model, and discuss natural extensions of our model to all other dimensions.

Much like the spontaneous breaking of the spatial translation defines an ordinary crystal, the spontaneous breaking of time translation characterizes novel phases of matter termed *time crystals* [1, 2]. Since the initial proposals, much effort has been devoted to understanding the properties of time-crystalline order and under what conditions it can occur [3–11]. Two broad questions motivate these explorations: what fundamentally determines the stability of a time crystal, and what is the nature of the long-lived subharmonic response?

When equations of motion are periodic in time, the corresponding discrete time crystal (DTC) is characterized by a robust and long-lived oscillation whose period is a multiple of the drive's [5–7, 12–21]. In this setting, the stability of a DTC is predicated on the system's failure to equilibrate across all of the phase space, a particularly challenging feat owing to interacting systems' natural "tendency to be ergodic" [22–26]. One approach to overcome this challenge is to induce many-body localization (MBL) [27–32], which offers the possibility for stabilizing a DTC to arbitrary late time [5–7, 12–17]. The dimensionality and disorder requirements of MBL have motivated the search for other settings where out-of-equilibrium phenomena can be stabilized, perhaps not to infinity, but rather parametrically long times. The most well-known example is the prethermal discrete time crystal (PDTC) [18–21], where the lifetime of the prethermal regime can be exponentially controlled by the frequency of the driving protocol [33–36], offering a large time window for studying the time-crystalline order. One big challenge is to understand under which settings this methodology can be extended.

Another dimension for characterizing DTCs is the nature of observables that exhibit robust oscillations. While the initial proposals involve spontaneous symmetry broken (SSB) systems where time-crystalline orders are observed in local observables throughout the whole system [5–8, 12–21], it has been recently proposed and experimentally observed, that the same machinery can be ported to symmetry-

protected topological (SPT) case or intrinsic topological order case, where different topological sectors are connected under the drive [37–39]. These examples demonstrate that time-

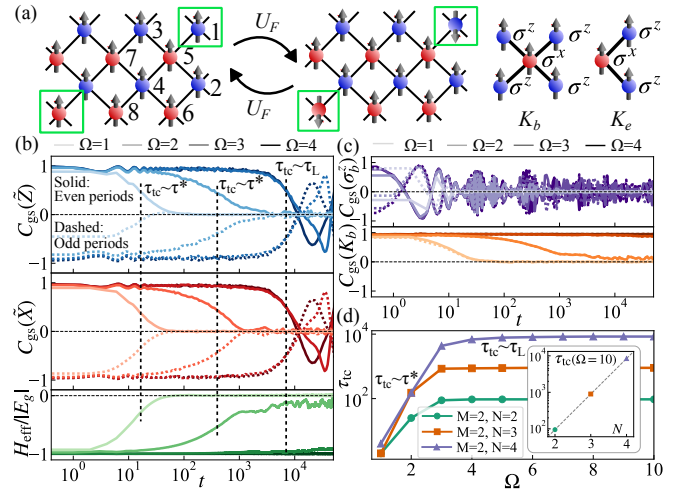


FIG. 1. **(a)** System composed of a checkerboard lattice with 1/2-spins living on red and blue sublattices, and stabilizer operators K_i in bulk and at edges. Corners spins (green boxes) exhibit a subharmonic response under the Floquet unitary U_F . **(b)** Dynamics of the autocorrelation functions for corner mode operators \tilde{Z} , \tilde{X} , and energy density with different drive frequencies. The initial state is the ground state of H_{eff} . With low drive frequency ($\Omega = 1, 2$), the time-crystalline lifetime τ_{tc} matches the heating time τ^* . With high drive frequency ($\Omega = 3, 4$), τ_{tc} is bounded by finite-size hybridization time τ_L . **(c)** Dynamics of the autocorrelation functions for σ^z in the bulk which shows a beating behavior, and the stabilizer in the bulk which has the same periodicity as $H(t)$. **(d)** The time-crystalline lifetime τ_{tc} under varying drive frequencies and system sizes. The inset shows the exponential scaling of τ_{tc} with the distance between two corners under a high-frequency drive. These numerical results are obtained with $J = 1$, $V_{xx} = 0.31$, $V_{zz} = 0.15$, $\epsilon = 0.05$, $h_x = 0.21$, $h_y = 0.17$, $h_z = 0.19$.

crystalline responses can be restricted into subsystems. However, since topological orders do not exist in finite temperature in two-dimensional (2D) and three-dimensional stabilizer codes [40, 41], one needs to prepare the systems' ground states to observe the robust subharmonic responses, which poses a stringent constraint on the initial states.

In this work, led by these two questions above, we discover a new kind of DTC phenomenon. In particular, we construct a 2D Floquet system where the time translation symmetry is only broken in zero-dimensional subsystems (i.e. at its corners). The localized nature of these corners offers a new avenue for their late-time stabilization using the physics of prethermal strong zero modes (PSZMs) [42–48]. This removes any requirements on the energy density of the initial states [Table. I]. Our results are threefold. First, we show that under high-frequency driving, a higher-order symmetry-protected topological (HOSPT) phase [49–57] emerges in the effective prethermal description. This phase gives rise to distinct gapless corner modes in the ground state manifold which exhibit long-lived subharmonic responses. Owing to the slow Floquet heating, the responses survive until an exponentially long heating time τ^* in the drive frequency. Second, we observe that, while these corner modes are only topologically protected in the ground-state manifold and destroyed at finite temperature, the decay of corners into bulk is highly suppressed in a *dimerized* version of our model. This provides a distinct mechanism for the stabilization of long-lived time-crystalline order that extends to arbitrary initial states (i.e. finite temperature) and for an exponentially long time, controlled by the degree of dimerization. Third, building upon the intuition in the 2D model, we discuss how to extend our results to arbitrary spatial dimensions and analyze how these time-crystalline dynamics can be realized on current superconducting quantum processors.

HOSPT-PDTC at zero temperature.—We consider a checkerboard lattice where spins-1/2 reside on two $N \times M$ sublattices [red and blue, Fig. 1(a)] evolving under the following time-periodic Hamiltonian $H(t) = H(t + T)$:

$$H(t) = \begin{cases} \sum_i \left(\frac{\pi}{T} + \epsilon \right) \sigma_i^x & 0 < t \leq \frac{T}{2} \\ J \sum_{i \notin \text{corner}} K_i + V(t) & \frac{T}{2} < t \leq T \end{cases} \quad (1)$$

Here, ϵ represents the imperfection of the π -pulse, and $K_i \equiv \sigma_i^x \prod_{\langle ji \rangle} \sigma_j^z$ is a multi-body stabilizer operator with $[K_a, K_b] = 0$, where $\langle ji \rangle$ denotes the spins j that are neighbors of spin i . The stabilizer term $\propto \sum_{i \notin \text{corner}} K_i$ is a cluster model that features a HOSPT phase in its ground state protected by the spin-flip symmetry $\prod_i \sigma_i^x$ on both red and blue sites, denoted by $\mathbb{Z}_2^{(b)} \times \mathbb{Z}_2^{(r)}$ [54, 57, 58]. $V(t)$ is a generic interacting perturbation that respects, at least, $\mathbb{Z}_2^{(b)}$ or $\mathbb{Z}_2^{(r)}$. Throughout this work, we consider

$$V(t) = JK_1 + h_x \sum_i \sigma_i^x + \sum_{i \in \text{red}} (h_y \sigma_i^y + h_z \sigma_i^z) + V_{xx} \sum_{\langle i,j \rangle} \sigma_i^x \sigma_j^x + V_{zz} \sum_i P_i, \quad (2)$$

TABLE I. Different mechanisms for stabilizing a discrete time crystal in an isolated Floquet system. We explore time-crystalline order stabilized via prethermal higher-order symmetry-protected topological (HOSPT) phases at zero temperature (Fig. 1), and via prethermal almost strong zero modes at finite temperature (Fig. 3).

Mechanism	MBL	Prethermalization	Prethermal strong zero modes
Origin of ergodicity breaking	ℓ -bits	Emergent symmetry	Local obstruction to equilibrium
Observable	Local observables (SSB) Edge modes [(HO)SPT]		0D Corner modes
Lifetime	∞	e^{Ω/Ω_0}	e^{J/J_0}
Dimension	Uncertain for $d > 1$	Arbitrary dimension	
Initial state	Any	Below T_c (SSB) $T = 0$ [(HO)SPT]	Any

where $P_i = \prod_{j \in \square_i} \sigma_j^z$ are four-body plaquette terms in bulk or two-body terms at edges [58]. We note that $V(t)$ explicitly breaks $\mathbb{Z}_2^{(r)}$ and thus the HOSPT phase is destroyed.

When the driving frequency $\Omega = 2\pi/T$ is much larger than any local energy scale Ω_0 , the system's dynamics under one period, $U_F = \mathcal{T} e^{-i \int_0^T H(t) dt}$, is well approximated by the evolution under an effective static Hamiltonian H_{eff} , followed by a perfect spin-flip $G = \prod_i \sigma_i^x = G_r G_b$. Crucially, although $\mathbb{Z}_2^{(r)}$ is not a symmetry of the underlying dynamics, it is a symmetry of the effective Hamiltonian, $[H_{\text{eff}}, G_r] = 0$, which is protected by the time-translation symmetry of the drive [19, 20]. The ability of H_{eff} to describe the system's dynamics is determined by the exponentially small error $O(e^{-\Omega/\Omega_0})$ in this approximation. This error is thought of as the source of heating to H_{eff} and, thus, determines an exponentially long prethermal window for $t < \tau^* \sim e^{\Omega/\Omega_0}$, where the system reach prethermal equilibrium with respect to H_{eff} :

$$2H_{\text{eff}} = J \sum_{i \notin \text{corner}} K_i + V_{zz} \sum_i P_i + V_{xx} \sum_{\langle i,j \rangle} \sigma_i^x \sigma_j^x + (h_x + \epsilon) \sum_i \sigma_i^x + O\left(\frac{\Omega_0}{\Omega}\right). \quad (3)$$

When $V(t) = 0$, H_{eff} exhibits an exactly four-fold degeneracy of the ground-state manifold, corresponding to the presence of two gapless corner spin-1/2 modes. One of them is exactly localized at spin 1 [Fig. 1(a)] and is characterized by two conjugate operators $\tilde{Z} = \sigma_1^z$ and $\tilde{X} = \sigma_1^x \sigma_5^z = K_1$. With non-zero perturbations $V(t)$, the corner mode becomes delocalized over a certain correlation length ξ . Under the periodic drive, the time evolution under H_{eff} preserves these corner modes, but the G rotation flips both associated edge modes ($G\tilde{Z}G = -\tilde{Z}$ and $G\tilde{X}G = -\tilde{X}$). This induces a subharmonic response with the corner spin changing sign for each period, which is the defining feature of a PDTC.

Indeed, this is borne out by our numerical simulations.

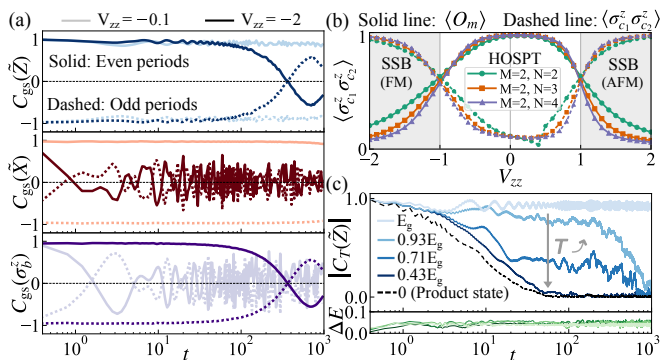


FIG. 2. The melting of a HOSPT-PDTC. (a) When $|V_{zz}|$ is large, the time-crystalline behavior for \tilde{X} is lost, and long-lived subharmonic responses occur for σ^z at corners, edges, and in bulk, which indicates the system transits to an SSB-PDTC. (b) Characterizing the transition between HOSPT-PDTCs and SSB-PDTCs by membrane operator $\langle O_m \rangle$ and correlator at two blue corners $\langle \sigma_{c_1}^z \sigma_{c_2}^z \rangle$. The crossings indicate two transition points around $V_{zz} = \pm 1$. (c) The HOSPT-PDTC quickly melts when the initial state is not the ground state, even if the system has not thermalized yet.

Starting the system in the ground state of H_{eff} , we compute the Floquet dynamics of Eq. (1) with small ϵ , h_x , V_{xx} and V_{zz} under different drive frequencies [Fig. 1(b)]. For small frequencies ($\Omega = 1$, light curves), the rapid heating induces the fast decay of the autocorrelation functions $C_{gs}(\tilde{Z}) = \text{Re}\langle \psi_{gs} | \tilde{Z}(t) \tilde{Z}(0) | \psi_{gs} \rangle$, $C_{gs}(\tilde{X})$ and energy density. By contrast, at high frequencies ($\Omega = 4$, dark curves), the system does not thermalize after a very long time ($\tau^* > 10^4$); until then, $C_{gs}(\tilde{Z})$ and $C_{gs}(\tilde{X})$ exhibits a long-lived subharmonic response, consistent with conjugate corner modes whose responses lock to the subharmonic frequency $\omega/\Omega = 1/2$.

A few remarks are in order. First, the importance of the higher-order nature of the PDTC can be further emphasized by contrasting the dynamics of corners with either edges or bulk. Instead of a robust subharmonic oscillation, $C_{gs}(\sigma_{e/b}^z)$ develops a strong beating behavior [Fig. 1(c)], whose frequency is controlled by the precise parameters of the system (for more details in [58]). In addition, $C_{gs}(K_{e/b})$ features a periodicity matching that of $H(t)$. Second, while in the thermodynamic limit, we expect the time-crystalline lifetime τ_{ic} to match the exponentially growing heating time scale τ^* , in a finite-size system, the hybridization of the corner modes upper bounds τ_{ic} . This hybridization arises from the exponentially small overlap between the localized corner modes and induces an exponentially small gap $\Delta_{\text{FS}} \sim e^{-L/\xi}$ between different states of the ground state manifold, where L is the distance between two corners. This manifests itself in the dynamics of the autocorrelation function of the corner modes, which exhibits a long, coherent oscillation with a time scale $\tau_L \sim 1/\Delta_{\text{FS}}$. Computing the frequency dependence of τ_{ic} demonstrates this phenomenon: after an initial exponential scaling e^{Ω/Ω_0} , τ_{ic} plateaus to a size-dependent value that is exponentially controlled by the distance [Fig. 1(d)].

Melting of a HOSPT-PDTC.—The observed subharmonic

response is robust to all kinds of perturbations in $V(t)$, as long as they preserve time-translation symmetry and the original $\mathbb{Z}_2^{(b)}$ symmetry. However, upon a large increase of either h_x , V_{xx} or V_{zz} , H_{eff} undergoes a quantum phase transition to a topologically trivial state, and the robustness of the corner modes is lost. We analyze this effect in detail when tuning V_{zz} [Fig. 2(a)], leaving the remaining perturbations to the Supplementary Materials [58]. When $|V_{zz}|$ is small (light curves), both conjugate operators \tilde{X} and \tilde{Z} exhibit robust time-crystalline behavior. Upon increasing V_{zz} (dark curve), the dynamics become different; while $C_{gs}(\tilde{X})$ becomes fast decaying, $C_{gs}(\tilde{Z})$ can still exhibit a long-lived subharmonic response. In large V_{zz} limit, H_{eff} supports ferromagnetic order (breaking \mathbb{Z}_2 symmetry) which stabilizes the observed sub-harmonic response. We verify this picture by studying the response of the bulk and edge degrees of freedom and we observe that $C_{gs}(\sigma_{e/b}^z)$ and $C_{gs}(\tilde{Z})$ exhibit an equally long-lived behavior. At the same time, the ground state phase diagram of H_{eff} as a function of V_{zz} precisely exhibits a phase transition from a HOSPT phase to a ferromagnet at $V_{zz} = -1$ [Fig. 2(b)], mirroring the transition from a HOSPT-PDTC to a SSB-PDTC [Table. I]. Curiously, the locations of the transition are exactly pinned at $V_{zz} = \pm 1$ owing to a self duality of the model [58].

One key ingredient in our discussions so far is that the system is initially prepared at zero temperature with respect to H_{eff} . Indeed, the topological protection of the gapless corner modes only exists within the ground state manifold [40, 41]. At finite temperature (i.e. higher energy density), thermal excitations from the bulk interact with these corner modes and lead to their decay. As a result, even if the heating time scale of the system is very large, the time-crystalline behavior can exhibit a fast decay [Fig. 2(c)].

Prethermal strong zero modes in a HOSPT-PDTC.—While the decay of the corner modes into the bulk is a generic feature at non-zero temperature, this process is highly constrained by the symmetry properties of our model. More specifically, the decay mainly arises from the energy exchange between stabilizer excitations at different sublattices. This observation suggests a simple, yet powerful path towards the extension of the time-crystalline lifetime of the corner modes: By changing the relative strength of stabilizers between the two sublattices, i.e., by *dimerizing* our model from J to J_r and J_b , the resonant process becomes suppressed and the corner modes become long-lived, regardless of the initial states. This long lifetime signals the formation of PSZMs [42–48].

The effectiveness of this dimerization strategy is best understood upon a dual transformation of H_{eff} [58–61]. The resulting dual model corresponds to two coupled plaquette Ising models, one for each sublattice:

$$2H_{\text{dual}} = J_r \sum_{i \in \text{red}} P_i + J_b \sum_{i \in \text{blue}} P_i + V_{zz} \sum_{i \notin \text{corner}} K_i + V_{xx} \sum_{\langle i,j \rangle} \sigma_i^x \sigma_j^x + (h_x + \epsilon) \sum_i \sigma_i^x + O\left(\frac{\Omega_0}{\Omega}\right). \quad (4)$$

With respect to the corner spins, the duality transformation maps them as follows: $\hat{Z} \rightarrow \hat{Z}_{\text{dual}} = \sigma_1^z G_r$ and $\hat{X} \rightarrow \hat{X}_{\text{dual}} = \sigma_5^z$, where $\sigma_{1,5}^z$ are at corners of the blue and red sublattices respectively. Crucially, because G_r commutes with the approximate Floquet evolution, the dynamics of \hat{Z}_{dual} are solely determined by the dynamics of σ_1^z [62]. The robustness of the original corner operators is then mapped to the robustness of the magnetization of the two corner spins, which is easier to analyze because we only need to consider spin-flip processes.

The effect of the coupling between the two sublattices becomes transparent in this language. Since a spin flip at corners either creates or destroys an odd number of plaquette excitations, when J_r and J_b are much larger than any other local energy scale J_0 , this process becomes exponentially suppressed owing to the emergence conservation of excitation number [35]. However, if we further add symmetry-preserved coupling between two sublattices (i.e. V_{xx} terms), the process of flipping both corner spins at two sublattices can be resonant. For example, $\sigma_1^x \sigma_5^x$ flips one $J_r P_i$ term and three $J_b P_i$ terms (one in bulk and two at edge). The resulting energy difference in the red sites is $2J_r$, and in the blue sites it is either $2J_b$ or $6J_b$ (depending on the particular spin configuration) [63]. Therefore, when $J_r = J_b$ or $J_r = 3J_b$, the process becomes resonant and the interaction strongly hybridizes the corners of different sublattices, which dominantly controls the corner modes' lifetime. Crucially, when these resonant conditions are not met, the plaquette excitation number for each sublattice becomes approximately conserved, which will greatly enhance the corner spins' lifetime.

The above understanding is clearly demonstrated by our numerical investigations [Fig. 3(a)]. When studying the dynamics under a dimerization strength $\eta \equiv J_r/J_b \neq 1$, we observe a large enhancement of the lifetime of the corner's subharmonic response, even when starting from a product state in the middle of the spectrum [Fig. 3(a)]. In contrast, for spins at the edge or in the bulk, the lifetime remains almost unchanged as the excitations can move freely among these spins without changing the total excitation numbers.

It is important to contrast the nature of the protection of the corner modes between the non-dimerized (Fig. 1) and dimerized (Fig. 3) cases. In the former, the robustness of the corners arises from the presence of topologically protected gapless modes in the ground state manifold. As long as the initial state has a large overlap with the ground state of H_{eff} , the lifetime of the time-crystalline behavior is limited by the heating time of the system $\tau_{\text{tc}} \sim e^{\Omega/\Omega_0}$. In contrast, the dimerization induces an *energetic barrier* to the process that leads to the decay of the corners, and, thus, is not restricted to the ground state manifold. In this case, the lifetime of the corners is limited by not only the heating time scale but also how well the dynamical constraint is satisfied, which (up to resonant conditions) can also be exponentially controlled [42, 43, 46]. The resulting lifetime is then upper bounded by $\tau_{\text{tc}} \sim \min\{e^{\Omega/\Omega_0}, e^{J_r/J_b}, e^{\min(J_r, J_b)/J_0}\}$.

In addition, the corner modes can be described by exact operators that commute, order by order, with H_{eff} . This further

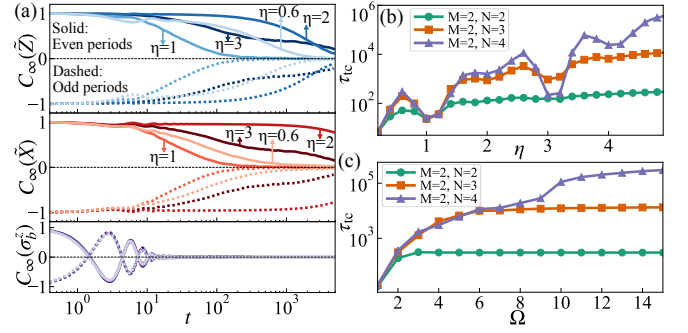


FIG. 3. The prethermal strong zero modes in a HOSPT-PDTC at finite temperature. (a) Starting from a product state with all spins pointing towards \hat{z} , the lifetime for the subharmonic responses at corners is extended by several orders of magnitude through dimerizing relative energy scales between different sublattices, while the lifetime for edge and bulk degrees of freedom is not enhanced. (b) The time-crystalline lifetime τ_{tc} under different dimerization strengths and system sizes with large-frequency drive ($\Omega = 20$). τ_{tc} first increases with η and then saturates due to the finite system size. Two dips occur at $\eta = 1, 3$ due to the resonance. (c) τ_{tc} under different drive frequencies and system sizes with $\eta = 5.11$. These results are obtained with $J_b = 1$, $V_{xx} = 0.11$, $V_{zz} = 0.05$, $h_x = 0.11$.

emphasizes the emergence of an approximately conserved quantity that constrains the system dynamics. Starting with the zeroth-order term $\Psi_z^{(0)} = \hat{Z}$, we consider perturbations of $h_x + \epsilon$, V_{xx} and V_{zz} , which results in the first-order term:

$$\Psi_z^{(1)} = \frac{h_x + \epsilon}{J_r} \Lambda_X + \frac{\eta^3}{(\eta^2 - 1)(\eta^2 - 9)} \frac{V_{xx}}{J_b} \Lambda_{XX}, \quad (5)$$

where Λ_X and Λ_{XX} consist of Pauli operators of spins around the corner [64], and the effect of V_{zz} appears in higher-order terms. Curiously, $\Psi_z^{(1)}$ already encodes the information about the aforementioned resonances: $\Psi_z^{(1)}$ diverges when $\eta = 1$ and 3 , which signals the breakdown of the perturbation analysis. Performing our analysis to higher-order uncovers additional higher-order resonant processes for particular values of η which further limit the corner mode lifetimes. These higher-order resonances are visible in our analysis of the system's corner mode lifetimes [Fig. 3(b)], with the emergence of dips in the lifetime at rational η . Nevertheless, unless the interaction terms are tuned to these rational values, this perturbative approach predicts exponentially long lived corner modes, controlled by the strength of the perturbative terms [33, 42, 65]. Indeed, for large η , $\tau_{\text{tc}}(\Omega)$ exhibits a similar behavior as the zero-temperature case [Fig. 3(c)], only being limited at large frequencies by system size hybridization of the corner modes.

We conclude our work by discussing future directions based on our results. First, despite the multi-body nature of the stabilizer terms in our model, recent developments in superconducting qubit arrays have enabled the digital simulation of Floquet dynamics of complex correlated systems [14, 15, 37, 39, 66]. Building upon these developments, we propose an experimental protocol for the observation of these long-lived corner modes [58]. Second, while we have focused our atten-

tion on a 2D model, our results can be easily extended into higher spatial dimensions. In this case, the n -dimensional stabilizer is defined on a hypercube, with a σ^x at its center and a σ^z operator for each of its corners. The analogous stabilizers at m -dimensional edges will have $2^m \sigma^z$ terms. Crucially, all but the $m = 0$ corner stabilizers will preserve the $\mathbb{Z}_2 \times \mathbb{Z}_2$ symmetry. As a result, the dynamically induced \mathbb{Z}_2 symmetry will cancel these corner stabilizers (in the high-frequency limit) and generate gapless corner modes. In 1D, this construction corresponds to the “ZXZ” chain, which features an SPT phase for its ground state with two edge modes [67, 68].

Third, we note that the discussed PSZMs are not unique to HOSPT phases, but also exist in Kitaev chains, XYZ chains, and at interfaces between different systems and phases [42, 44, 69]. It is then interesting if there exist novel features in time-crystalline orders of these systems. Finally, the Floquet driving in our scenario generates only one \mathbb{Z}_2 symmetry, necessitating the underlying dynamics to respect another \mathbb{Z}_2 symmetry. However, it is known that a quasi-periodic drive can generate multiple symmetries, offering a path for generating the fully required $\mathbb{Z}_2 \times \mathbb{Z}_2$ symmetry [70–74]. This comes at the cost of more complex Floquet heating dynamics. Understanding how the interplay of these effects affects the stability of the corner modes remains an open question.

We gratefully acknowledge the discussions with Jack Kemp about the prethermal strong zero modes, with Yong Xu and Kai Li about the higher-order symmetry-protected topological phases. The numerical simulations performed in this work are based on the dynamite [75] and Cirq [76] package written in Python. S.J., D. Y., W. J., and D.-L.D. acknowledge support from the National Natural Science Foundation of China (Grant Nos. T2225008, 12075128 and 123B2072), the Innovation Program for Quantum Science and Technology (Grant No. 2021ZD0302203), Tsinghua University Dushi Program, and Shanghai Qi Zhi Institute. F.M. acknowledges support from the NSF through a grant for ITAMP at Harvard University.

* dldeng@tsinghua.edu.cn

† francisco.leal_machado@cfa.harvard.edu

- [1] F. Wilczek, “Quantum time crystals,” *Phys. Rev. Lett.* **109**, 160401 (2012).
- [2] A. Shapere and F. Wilczek, “Classical time crystals,” *Phys. Rev. Lett.* **109**, 160402 (2012).
- [3] P. Bruno, “Impossibility of spontaneously rotating time crystals: A no-go theorem,” *Phys. Rev. Lett.* **111**, 070402 (2013).
- [4] H. Watanabe and M. Oshikawa, “Absence of quantum time crystals,” *Phys. Rev. Lett.* **114**, 251603 (2015).
- [5] V. Khemani, A. Lazarides, R. Moessner, and S. L. Sondhi, “Phase structure of driven quantum systems,” *Phys. Rev. Lett.* **116**, 250401 (2016).
- [6] D. V. Else, B. Bauer, and C. Nayak, “Floquet time crystals,” *Phys. Rev. Lett.* **117**, 090402 (2016).
- [7] N. Y. Yao, A. C. Potter, I.-D. Potirniche, and A. Vishwanath, “Discrete time crystals: Rigidity, criticality, and realizations,” *Phys. Rev. Lett.* **118**, 030401 (2017).
- [8] K. Sacha and J. Zakrzewski, “Time crystals: a review,” *Rep. Prog. Phys.* **81**, 016401 (2017).
- [9] V. Khemani, R. Moessner, and S. L. Sondhi, “A Brief History of Time Crystals,” [arXiv:1910.10745](https://arxiv.org/abs/1910.10745).
- [10] D. V. Else, C. Monroe, C. Nayak, and N. Y. Yao, “Discrete time crystals,” *Annu. Rev. Condens. Matter Phys.* **11**, 467 (2020).
- [11] M. P. Zaletel, M. Lukin, C. Monroe, C. Nayak, F. Wilczek, and N. Y. Yao, “Colloquium: Quantum and classical discrete time crystals,” *Rev. Mod. Phys.* **95**, 031001 (2023).
- [12] J. Zhang, P. W. Hess, A. Kyprianidis, P. Becker, A. Lee, J. Smith, G. Pagano, I.-D. Potirniche, A. C. Potter, A. Vishwanath, N. Y. Yao, and C. Monroe, “Observation of a discrete time crystal,” *Nature* **543**, 217 (2017).
- [13] S. Choi, J. Choi, R. Landig, G. Kucsko, H. Zhou, J. Isoya, F. Jelezko, S. Onoda, H. Sumiya, V. Khemani, C. von Keyserlingk, N. Y. Yao, E. Demler, and M. D. Lukin, “Observation of discrete time-crystalline order in a disordered dipolar many-body system,” *Nature* **543**, 221 (2017).
- [14] X. Mi, M. Ippoliti, C. Quintana, A. Greene, Z. Chen, J. Gross, *et al.*, “Time-crystalline eigenstate order on a quantum processor,” *Nature* **601**, 531 (2021).
- [15] P. Frey and S. Rachel, “Realization of a discrete time crystal on 57 qubits of a quantum computer,” *Sci. Adv.* **8**, eabm7652 (2022).
- [16] S. Pal, N. Nishad, T. S. Mahesh, and G. J. Sreejith, “Temporal order in periodically driven spins in star-shaped clusters,” *Phys. Rev. Lett.* **120**, 180602 (2018).
- [17] J. Rovny, R. L. Blum, and S. E. Barrett, “Observation of discrete-time-crystal signatures in an ordered dipolar many-body system,” *Phys. Rev. Lett.* **120**, 180603 (2018).
- [18] T.-S. Zeng and D. N. Sheng, “Prethermal time crystals in a one-dimensional periodically driven floquet system,” *Phys. Rev. B* **96**, 094202 (2017).
- [19] D. V. Else, B. Bauer, and C. Nayak, “Prethermal phases of matter protected by time-translation symmetry,” *Phys. Rev. X* **7**, 011026 (2017).
- [20] F. Machado, D. V. Else, G. D. Kahanamoku-Meyer, C. Nayak, and N. Y. Yao, “Long-range prethermal phases of nonequilibrium matter,” *Phys. Rev. X* **10**, 011043 (2020).
- [21] A. Kyprianidis, F. Machado, W. Morong, P. Becker, K. S. Collins, D. V. Else, L. Feng, P. W. Hess, C. Nayak, G. Pagano, N. Y. Yao, and C. Monroe, “Observation of a prethermal discrete time crystal,” *Science* **372**, 1192 (2021).
- [22] T. c. v. Prosen, “Time evolution of a quantum many-body system: Transition from integrability to ergodicity in the thermodynamic limit,” *Phys. Rev. Lett.* **80**, 1808 (1998).
- [23] T. c. v. Prosen, “Ergodic properties of a generic nonintegrable quantum many-body system in the thermodynamic limit,” *Phys. Rev. E* **60**, 3949 (1999).
- [24] A. Lazarides, A. Das, and R. Moessner, “Equilibrium states of generic quantum systems subject to periodic driving,” *Phys. Rev. E* **90**, 012110 (2014).
- [25] L. D. Marin Bukov and A. Polkovnikov, “Universal high-frequency behavior of periodically driven systems: from dynamical stabilization to floquet engineering,” *Adv. Phys.* **64**, 139 (2015).
- [26] L. D’Alessio and M. Rigol, “Long-time behavior of isolated periodically driven interacting lattice systems,” *Phys. Rev. X* **4**, 041048 (2014).
- [27] R. Nandkishore and D. Huse, “Many-body localization and thermalization in quantum statistical mechanics,” *Annu. Rev. Condens. Matter Phys.* **6**, 15 (2014).
- [28] J. A. Kjäll, J. H. Bardarson, and F. Pollmann, “Many-body

- localization in a disordered quantum ising chain,” *Phys. Rev. Lett.* **113**, 107204 (2014).
- [29] P. Ponte, A. Chandran, Z. Papić, and D. A. Abanin, “Periodically driven ergodic and many-body localized quantum systems,” *Ann. Phys.* **353**, 196 (2015).
- [30] D. A. Abanin, E. Altman, I. Bloch, and M. Serbyn, “Colloquium: Many-body localization, thermalization, and entanglement,” *Rev. Mod. Phys.* **91**, 021001 (2019).
- [31] P. Ponte, Z. Papić, F. m. c. Huvneers, and D. A. Abanin, “Many-body localization in periodically driven systems,” *Phys. Rev. Lett.* **114**, 140401 (2015).
- [32] A. Lazarides, A. Das, and R. Moessner, “Fate of many-body localization under periodic driving,” *Phys. Rev. Lett.* **115**, 030402 (2015).
- [33] D. A. Abanin, W. De Roeck, and F. m. c. Huvneers, “Exponentially slow heating in periodically driven many-body systems,” *Phys. Rev. Lett.* **115**, 256803 (2015).
- [34] T. Kuwahara, T. Mori, and K. Saito, “Floquet–magnus theory and generic transient dynamics in periodically driven many-body quantum systems,” *Ann. Phys.* **367**, 96 (2016).
- [35] D. Abanin, W. D. Roeck, W. W. Ho, and F. Huvneers, “A rigorous theory of many-body prethermalization for periodically driven and closed quantum systems,” *Commun. Math. Phys.* **354**, 809 (2017).
- [36] T. Mori, “Floquet prethermalization in periodically driven classical spin systems,” *Phys. Rev. B* **98**, 104303 (2018).
- [37] X. Zhang, W. Jiang, J. Deng, K. Wang, J. Chen, P. Zhang, W. Ren, H. Dong, S. Xu, Y. Gao, *et al.*, “Digital quantum simulation of floquet symmetry-protected topological phases,” *Nature* **607**, 468 (2022).
- [38] T. B. Wahl, B. Han, and B. Béri, “Topologically ordered time crystals,” [arXiv:2105.09694](https://arxiv.org/abs/2105.09694).
- [39] L. Xiang, W. Jiang, Z. Bao, Z. Song, S. Xu, K. Wang, J. Chen, F. Jin, *et al.*, “Long-lived topological time-crystalline order on a quantum processor,” [arXiv:2401.04333](https://arxiv.org/abs/2401.04333).
- [40] B. Yoshida, “Feasibility of self-correcting quantum memory and thermal stability of topological order,” *Ann. Phys.* **326**, 2566–2633 (2011).
- [41] S. Bravyi and B. Terhal, “A no-go theorem for a two-dimensional self-correcting quantum memory based on stabilizer codes,” *New J. Phys.* **11**, 043029 (2009).
- [42] J. Kemp, N. Y. Yao, C. R. Laumann, and P. Fendley, “Long coherence times for edge spins,” *J. Stat. Mech.* **2017**, 063105 (2017).
- [43] D. V. Else, P. Fendley, J. Kemp, and C. Nayak, “Prethermal strong zero modes and topological qubits,” *Phys. Rev. X* **7**, 041062 (2017).
- [44] P. Fendley, “Strong zero modes and eigenstate phase transitions in the xyz/interacting majorana chain,” *J. Phys. A* **49**, 30LT01 (2016).
- [45] D. E. Parker, R. Vasseur, and T. Scaffidi, “Topologically protected long edge coherence times in symmetry-broken phases,” *Phys. Rev. Lett.* **122**, 240605 (2019).
- [46] J. Kemp, N. Y. Yao, and C. R. Laumann, “Symmetry-enhanced boundary qubits at infinite temperature,” *Phys. Rev. Lett.* **125**, 200506 (2020).
- [47] D. J. Yates, A. G. Abanov, and A. Mitra, “Long-lived period-doubled edge modes of interacting and disorder-free floquet spin chains,” *Commun. Phys.* **5**, 43 (2022).
- [48] B. Mukherjee, R. Melendrez, M. Szyniszewski, H. J. Changlani, and A. Pal, “Emergent strong zero mode through local floquet engineering,” *Phys. Rev. B* **109**, 064303 (2024).
- [49] H. Isobe and L. Fu, “Theory of interacting topological crystalline insulators,” *Phys. Rev. B* **92**, 081304 (2015).
- [50] S.-J. Huang, H. Song, Y.-P. Huang, and M. Hermele, “Building crystalline topological phases from lower-dimensional states,” *Phys. Rev. B* **96**, 205106 (2017).
- [51] H. Song, S.-J. Huang, L. Fu, and M. Hermele, “Topological phases protected by point group symmetry,” *Phys. Rev. X* **7**, 011020 (2017).
- [52] Z. Song, Z. Fang, and C. Fang, “ $(d - 2)$ -dimensional edge states of rotation symmetry protected topological states,” *Phys. Rev. Lett.* **119**, 246402 (2017).
- [53] F. Schindler, A. M. Cook, M. G. Vergniory, Z. Wang, S. S. P. Parkin, B. A. Bernevig, and T. Neupert, “Higher-order topological insulators,” *Sci. Adv.* **4**, eaat0346 (2018).
- [54] Y. You, T. Devakul, F. J. Burnell, and T. Neupert, “Higher-order symmetry-protected topological states for interacting bosons and fermions,” *Phys. Rev. B* **98**, 235102 (2018).
- [55] D. Călugăru, V. Juričić, and B. Roy, “Higher-order topological phases: A general principle of construction,” *Phys. Rev. B* **99**, 041301 (2019).
- [56] A. Rasmussen and Y.-M. Lu, “Classification and construction of higher-order symmetry-protected topological phases of interacting bosons,” *Phys. Rev. B* **101**, 085137 (2020).
- [57] O. Dubinkin and T. L. Hughes, “Higher-order bosonic topological phases in spin models,” *Phys. Rev. B* **99**, 235132 (2019).
- [58] See Supplemental Material for details on conjugate operators for corner modes, analysis of the system dynamics, the duality transformation, the melting of HOSPT-PDTCs by other perturbations, and the experimental proposal with superconducting qubits, which includes Refs. [77, 78].
- [59] T. Kennedy and H. Tasaki, “Hidden $z_2 \times z_2$ symmetry breaking in haldane-gap antiferromagnets,” *Phys. Rev. B* **45**, 304 (1992).
- [60] A. C. Doherty and S. D. Bartlett, “Identifying phases of quantum many-body systems that are universal for quantum computation,” *Phys. Rev. Lett.* **103**, 020506 (2009).
- [61] Y. You, T. Devakul, F. J. Burnell, and S. L. Sondhi, “Subsystem symmetry protected topological order,” *Phys. Rev. B* **98**, 035112 (2018).
- [62] Note that even if G_r does not affect the dynamics of the \tilde{Z}_{dual} , it is still necessary to define the appropriate commutation relations between \tilde{X}_{dual} and \tilde{Z}_{dual} .
- [63] Suppose σ_1^z is \downarrow and σ_5^z is \uparrow , then the only configuration of $\sigma_5^z \sigma_6^z \sigma_7^z \sigma_8^z$ which resonates with $J_r = 3J_b$ is $\uparrow\uparrow\uparrow$. For all the other configurations, they will resonate with $J_r = J_b$.
- [64] $\Lambda_X = \sigma_1^x \sigma_2^z \sigma_3^z \sigma_4^z \sigma_5^x$, $\Lambda_{XX} = -6\eta^{-3} \sigma_1^y \sigma_2^x \sigma_3^x \sigma_4^y \sigma_5^z \sigma_8^z + (7\eta^{-2} - 1) \sigma_1^x \sigma_2^z \sigma_3^z \sigma_4^z + (3\eta^{-3} - \eta^{-1}) \sigma_1^y \sigma_2^x \sigma_5^y \sigma_6^z + (3\eta^{-3} - \eta^{-1}) \sigma_1^y \sigma_3^z \sigma_4^y \sigma_7^z + 2\eta^{-2} \sigma_1^x \sigma_2^y \sigma_3^z \sigma_4^z \sigma_6^z \sigma_7^z + 2\eta^{-2} \sigma_1^x \sigma_2^z \sigma_3^y \sigma_4^z \sigma_6^z \sigma_8^z + 2\eta^{-2} \sigma_1^x \sigma_2^z \sigma_3^z \sigma_4^y \sigma_7^z \sigma_8^z + (3\eta^{-3} - \eta^{-1}) \sigma_1^y \sigma_4^x \sigma_5^y \sigma_6^z \sigma_7^z \sigma_8^z$.
- [65] D. A. Abanin, W. De Roeck, W. W. Ho, and F. m. c. Huvneers, “Effective hamiltonians, prethermalization, and slow energy absorption in periodically driven many-body systems,” *Phys. Rev. B* **95**, 014112 (2017).
- [66] X. Mi, M. Sonner, M. Y. Niu, K. W. Lee, B. Foxen, R. Acharya, I. Aleiner, T. I. Andersen, F. Arute, *et al.*, “Noise-resilient edge modes on a chain of superconducting qubits,” *Science* **378**, 785 (2022).
- [67] R. Raussendorf and H. J. Briegel, “A one-way quantum computer,” *Phys. Rev. Lett.* **86**, 5188 (2001).
- [68] X. Chen, Y.-M. Lu, and A. Vishwanath, “Symmetry-protected topological phases from decorated domain walls,” *Nat. Commun.* **5**, 3507 (2014).
- [69] C. T. Olund, N. Y. Yao, and J. Kemp, “Boundary strong zero modes,” [arXiv:2305.16382](https://arxiv.org/abs/2305.16382).
- [70] D. V. Else, W. W. Ho, and P. T. Dumitrescu, “Long-lived interacting phases of matter protected by multiple time-translation

- symmetries in quasiperiodically driven systems,” *Phys. Rev. X* **10**, 021032 (2020).
- [71] A. J. Friedman, B. Ware, R. Vasseur, and A. C. Potter, “Topological edge modes without symmetry in quasiperiodically driven spin chains,” *Phys. Rev. B* **105**, 115117 (2022).
- [72] P. T. Dumitrescu, R. Vasseur, and A. C. Potter, “Logarithmically slow relaxation in quasiperiodically driven random spin chains,” *Phys. Rev. Lett.* **120**, 070602 (2018).
- [73] P. T. Dumitrescu, J. G. Bohnet, J. P. Gaebler, A. Hankin, D. Hayes, A. Kumar, B. Neyenhuis, R. Vasseur, and A. C. Potter, “Dynamical topological phase realized in a trapped-ion quantum simulator,” *Nature* **607**, 463–467 (2022).
- [74] G. He, B. Ye, R. Gong, C. Yao, Z. Liu, K. W. Murch, N. Y. Yao, and C. Zu, “Experimental realization of discrete time quasi-crystals,” [arXiv:2403.17842](https://arxiv.org/abs/2403.17842).
- [75] G. D. Kahanamoku-Meyer and J. Wei, “Dynamite,” (2023), [Zenodo:10.5281/zenodo.3606825](https://zenodo.org/record/10.5281/zenodo.3606825).
- [76] Cirq Developers, “Cirq,” (2023), [Zenodo:10.5281/zenodo.8161252](https://zenodo.org/record/10.5281/zenodo.8161252).
- [77] C.-L. Deng, Y. Liu, Y.-R. Zhang, X.-G. Li, T. Liu, C.-T. Chen, T. Liu, *et al.*, “High-order topological pumping on a superconducting quantum processor,” [arXiv:2402.16070](https://arxiv.org/abs/2402.16070).
- [78] K. J. Satzinger, Y.-J. Liu, A. Smith, C. Knapp, M. Newman, C. Jones, Z. Chen, C. Quintana, X. Mi, A. Dunsworth, C. Gidney, *et al.*, “Realizing topologically ordered states on a quantum processor,” *Science* **374**, 1237 (2021).

Supplementary Materials: Prethermal Time-Crystalline Corner Modes

THE SYSTEM CONFIGURATIONS AND THEIR CORNER MODES

In the main text, we considered a system consisting of two sublattices of equal size ($N \times M$), such that each sublattice features a corner spin. We argue that this requirement can be relaxed; by choosing different sizes for the two sublattices, the system has different number of corner spins, all of which exhibit the same features discussed in the main text. Systems on the checkerboard lattice with rectangular shapes can be categorized into four groups, as shown in Fig. S1(a-d): (a) all sides of the rectangle reside on the same sublattice; (b) there are three adjacent sides residing on the same sublattice; (c) there are two adjacent sides residing on the same sublattice, and (d) all adjacent sides reside on different sublattices. Corner sites occur when there are adjacent sides reside on the same sublattice. Their stabilizer operators break the $\mathbb{Z}_2 \times \mathbb{Z}_2$ symmetry and will not occur in the prethermal effective Hamiltonian.

The degeneracy of the ground-state manifold can be computed by projecting the $\mathbb{Z}_2 \times \mathbb{Z}_2$ symmetry onto the corners (which also leads to the operators describing the corner modes). The symmetry generators $G_r = \prod_{i \in \text{red}} \sigma_i^x$, $G_b = \prod_{i \in \text{blue}} \sigma_i^x$ can be decomposed into the product of stabilizers and σ_i^z . Using the geometry shown in Fig. S1(a) as an example:

$$G_b = \prod_{i \in \text{blue}} K_i, \quad G_r = \prod_{i \in \text{red}} K_i \prod_{j \in \text{corner}} \sigma_j^z. \quad (\text{S1})$$

In the ground-state manifold of the fixed-point effective Hamiltonian (i.e. simple stabilizer Hamiltonian), these operators are further simplified by noting that the stabilizers at edges and in bulk take value -1 . As a result, the action of the symmetry generators in the ground state manifold is given by:

$$G_b \propto \prod_{i \in \text{corner}} K_i, \quad G_r \propto \prod_{i \in \text{corner}} \sigma_i^z. \quad (\text{S2})$$

Note that both generators are projected onto the corners, where K_i and σ_i^z anti-commute with one another. Because the effective Hamiltonian commutes with both G_r and G_b (by the $\mathbb{Z}_2 \times \mathbb{Z}_2$ symmetry), we immediately ensure that $[\prod_{i \in \text{corner}} \sigma_i^z, H_{\text{eff}}] = 0$ and $[K_i, H_{\text{eff}}] = 0$, which by locality of the Hamiltonian ensures that the corner modes $\tilde{Z} \equiv \sigma_i^z$ and $\tilde{X} \equiv K_i$ are integral of motions. Together with the fact that \tilde{X} and \tilde{Z} are anti-commuted, we conclude that the degeneracy of the ground state manifold is greater than 1, with the corner modes corresponding to the local operator that connects between the different ground states.

For the systems shown in Fig. S1(b-c), similar process can also be done. For (b) we also have

$$G_b \propto \prod_{i \in \text{corner}} K_i, \quad G_r \propto \prod_{i \in \text{corner}} \sigma_i^z, \quad (\text{S3})$$

and for (c),

$$G_b \propto K_{\text{b,c}} \sigma_{\text{r,c}}^z, \quad G_r \propto K_{\text{r,c}} \sigma_{\text{b,c}}^z \quad (\text{S4})$$

where $K_{\text{r,c}}, \sigma_{\text{r,c}}^z$ ($K_{\text{b,c}}, \sigma_{\text{b,c}}^z$) are located at the red (blue) corner. However, for the system in (d), the symmetry generators become

$$G_r = \prod_{i \in \text{red}} K_i \propto 1, \quad G_b = \prod_{i \in \text{blue}} K_i \propto 1, \quad (\text{S5})$$

where the whole system has a unique ground state and no gapless corner modes exist.

ANALYSING THE SYSTEM'S DYNAMICS

As we argue in the main text, the system's dynamics are given by $U_F = e^{-iH_{\text{eff}}T} G + O(e^{-\Omega/\Omega_0})$ with the effective Hamiltonian being given by:

$$2H_{\text{eff}} = J \sum_{i \notin \text{corner}} K_i + V_{zz} \sum_i P_i + V_{xx} \sum_{\langle i,j \rangle} \sigma_i^x \sigma_j^x + (h_x + \epsilon) \sum_i \sigma_i^x + O\left(\frac{\Omega_0}{\Omega}\right). \quad (\text{S6})$$

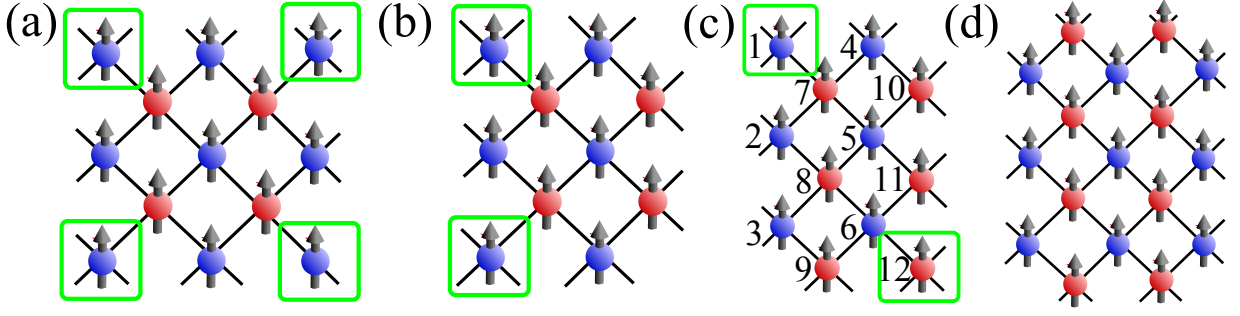


FIG. S1. Different configurations for systems with rectangular shapes on the checkerboard lattice. The corners, which are highlighted by the green boxes, occur at the intersections of adjacent sides residing on the same sublattice type.

In the prethermal regime (while $U_F \approx e^{-iH_{\text{eff}}T}$ is a valid approximation), the autocorrelation function of the ground state after n periods can be expressed, for any observable O , as

$$\begin{aligned} C_{\text{gs}}(O, nT) &= \langle \psi_0 | O(nT)O(0) | \psi_0 \rangle \\ &= \left\langle \psi_0 \left| \prod_{i=1}^n (G e^{iH_{\text{eff}}T}) O \prod_{i=1}^n (e^{-iH_{\text{eff}}T} G) O \right| \psi_0 \right\rangle \\ &= e^{iE_0 nT} \langle \psi_0 | G^n O G^n e^{-iH_{\text{eff}}nT} O | \psi_0 \rangle, \end{aligned} \quad (\text{S7})$$

where $|\psi_0\rangle$ is the ground state of H_{eff} and E_0 is the ground state energy. The last equation holds since $[G, H_{\text{eff}}] = 0$. Since the operator O we focus on either commutes or anti-commutes with G , we can define $G^n O G^n = f(O, n)O$ with

$$f(O, n) = \begin{cases} 1 & [O, G] = 0 \\ (-1)^n & \{O, G\} = 0 \end{cases}, \quad (\text{S8})$$

and the autocorrelation function is further simplified as

$$C_{\text{gs}}(O, nT) = f(O, n) e^{iE_0 nT} \langle \psi_0 | O e^{-iH_{\text{eff}}nT} O | \psi_0 \rangle. \quad (\text{S9})$$

The dynamics can be easily understood when the driving frequency is large ($\Omega_0/\Omega \rightarrow 0$) and there are no perturbation terms ($\epsilon = h_x = V_{xx} = V_{zz} = 0$). In this case, $H_{\text{eff}} = (J/2) \sum_{i \notin \text{corner}} K_i$ yields two exact gapless corner modes with four degenerated ground states. For \tilde{Z} and \tilde{X} which anti-commute with G and commute with H_{eff} , we have $f(O, n) = (-1)^n$ and $O e^{-iH_{\text{eff}}nT} O = O^2 e^{-iH_{\text{eff}}nT} = e^{-iH_{\text{eff}}nT}$, leading to

$$C_{\text{gs}}(\tilde{Z}, nT) = C_{\text{gs}}(\tilde{X}, nT) = (-1)^n, \quad (\text{S10})$$

which are subharmonic responses with $\omega/\Omega = \frac{1}{2}$. For stabilizers $K_{e/b}$ at edges and in bulk which commute to both G and H_{eff} , we have

$$C_{\text{gs}}(K_{e/b}, nT) = 1. \quad (\text{S11})$$

Situations change when we consider $\sigma_{e/b}^z$ which does not commute with H_{eff} . Concretely, at the edges and in bulk, σ_i^z anti-commutes with K_i , but commutes with all K_j with $j \neq i$. This leads to $e^{-iH_{\text{eff}}nT} \sigma_i^z = \sigma_i^z e^{-i(H_{\text{eff}} - JK_i)nT}$. Therefore, at edges and in bulk we have

$$C_{\text{gs}}(\sigma_i, nT) = (-1)^n e^{-iJnT}. \quad (\text{S12})$$

This is a rapid spin-flipping process modulated by a frequency determined by J , leading to the observed beating behavior, and thus **not** a robust sub-harmonic response.

Now we consider the case when the perturbation terms are not zero. We first decompose $O|\psi_0\rangle$ into eigenstates of H_{eff} , which gives $O|\psi_0\rangle = \sum_i \alpha_i |\psi_i\rangle$. Then the autocorrelation function shown in Eq. (S9) can be written as

$$\begin{aligned} C_{\text{gs}}(O, nT) &= f(O, n) e^{iE_0 nT} \sum_{i,j} \alpha_j^* \alpha_i e^{-iE_i nT} \langle \psi_j | \psi_i \rangle \\ &= f(O, n) \sum_i |\alpha_i|^2 e^{-i(E_i - E_0)nT} \end{aligned} \quad (\text{S13})$$

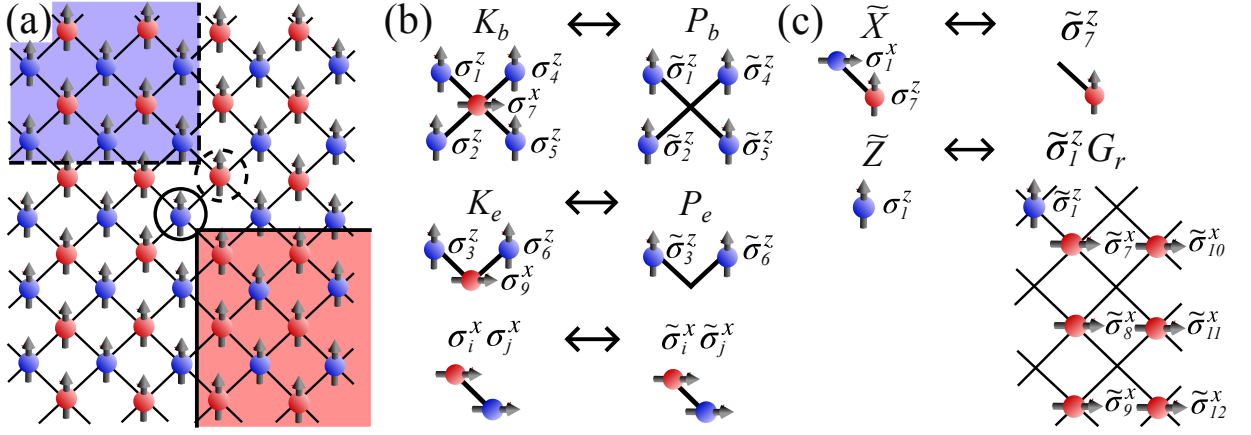


FIG. S2. The duality transformation. (a) The σ_i^z of a blue (red) spin is transformed into $\tilde{\sigma}_i^z$ times the product of $\tilde{\sigma}^x$ of the red (blue) spins in the red (blue) area A_r (A_b). (b) The stabilizer operators in bulk (at edges) and the four-body (two-body) plaquette terms are transformed into each other. The $V_{xx}\sigma_i^x\sigma_j^x$ terms are transformed into themselves. (c) The corner operator \tilde{X} is transformed into the $\tilde{\sigma}^z$ at the corner of the red sublattice, and \tilde{Z} is transformed into the $\tilde{\sigma}^z$ at the corner of the blue sublattice times the emergent symmetry G_r .

As long as the perturbations are small, $\tilde{Z}|\psi_0\rangle$ is very close to a system eigenstate $|\psi_j\rangle$ with $E_j - E_0 \sim \Delta_{\text{FS}}$, where Δ_{FS} is the finite-size energy gap occurring at the ground-state manifold due to the perturbations. Therefore, we have

$$C_{\text{gs}}(\tilde{Z}, nT) \approx (-1)^n e^{-i\Delta_{\text{FS}}nT}. \quad (\text{S14})$$

The same arguments can be carried out for $\tilde{X}|\psi_0\rangle$. This explains the very long, but finite system size lifetime τ_L observed in the main text.

THE DUALITY TRANSFORMATION

In Eq.(3) of the main text, we show that the stabilizer operators are transformed to plaquette Ising terms on two sublattices in a dual picture. We now describe this duality in more detail. This duality is well-known in the one-dimensional case, which generalizes the idea in [59] that transforms a Haldane-type $\mathbb{Z}_2 \times \mathbb{Z}_2$ chain into two Ising chains. The generalization of this duality into the two-dimensional case can be found in [60], which maps σ^x to itself:

$$\sigma_i^x \longleftrightarrow \tilde{\sigma}_i^x. \quad (\text{S15})$$

While for σ_i^z , the mapping depends on the color of spin i :

$$\sigma_i^z \longleftrightarrow \begin{cases} \tilde{\sigma}_i^z \prod_{j \in \text{red}, j \in A_r} \tilde{\sigma}_j^x, & i \in \text{blue} \\ \tilde{\sigma}_i^z \prod_{j \in \text{blue}, j \in A_b} \tilde{\sigma}_j^x, & i \in \text{red} \end{cases}, \quad (\text{S16})$$

where A_r contains all red spins located to the lower right of the spin i , and A_b contains all blue spins located to the upper left of i , as shown in Fig. S2(a).

With this duality transformation, we study how it acts on the prethermal effective Hamiltonian Eq. (S6). One can verify that the stabilizer operators K_i and the plaquette terms P_i are mapped to each other, while σ_i^x and $\sigma_i^x\sigma_j^x$ are mapped to themselves:

$$K_i = \sigma_i^x \prod_{\langle ji \rangle} \sigma_j^z \longleftrightarrow \prod_{\langle ji \rangle} \tilde{\sigma}_j^z = \tilde{P}_i, \quad (\text{S17})$$

$$\sigma_i^x \longleftrightarrow \tilde{\sigma}_i^x, \quad \sigma_i^x \sigma_j^x \longleftrightarrow \tilde{\sigma}_i^x \tilde{\sigma}_j^x. \quad (\text{S18})$$

We show concrete examples of transforming stabilizers in the bulk and at the edge in Fig. S2(b). Putting these results together, we obtain the effective Hamiltonian in the dual picture as

$$2H_{\text{dual}} = V_{zz} \sum_{i \notin \text{corner}} \tilde{K}_i + J \sum_i \tilde{P}_i + V_{xx} \sum_{\langle i,j \rangle} \tilde{\sigma}_i^x \tilde{\sigma}_j^x + (h_x + \epsilon) \sum_i \tilde{\sigma}_i^x + O\left(\frac{\Omega_0}{\Omega}\right). \quad (\text{S19})$$

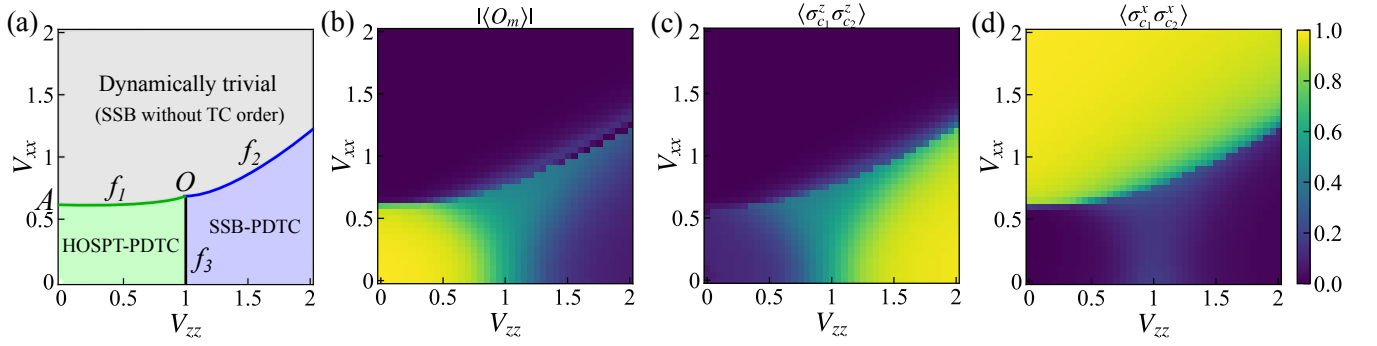


FIG. S3. (a) The phase diagram as a function of perturbation strengths V_{zz} and V_{xx} , where f_1, f_2, f_3 are the functions of phase boundaries, and O is the intersection point of three phases. (b-d) Numerical calculations for the order parameters of the (b) HOSPT-PDTCs, (c) SSB-PDTCs, and (d) dynamically trivial phase.

$J \sum_i \tilde{P}_i$ is now the dominant term in the Hamiltonian, which can be considered as plaquette Ising models on two sublattices. Note, that, by comparison with Eq. (S6), H_{eff} and H_{dual} have the same form, which tells us that H_{eff} is a self-dual model. This directly gives that the phase transition between the plaquette Ising model and the HOSPT, which originates from the competition between K_i and P_i , must occur at the self-dual point $V_{zz}/J = \pm 1$. This is in agreement with the observation of the HOSPT-PDTC to SSB-PDTC transition reported in the main text when $|V_{zz}| > |J|$.

We can also use this duality transformation to better understand the long lifetime of the corner modes. In the dual picture, the corner operators are mapped into

$$\tilde{X} = \sigma_1^x \sigma_7^z \longleftrightarrow \tilde{\sigma}_7^z \quad (\text{S20})$$

$$\tilde{Z} = \sigma_1^z \longleftrightarrow \tilde{\sigma}_1^z \prod_{i \in \text{red}} \tilde{\sigma}_i^x = \tilde{\sigma}_1^z \tilde{G}_r, \quad (\text{S21})$$

which are shown in Fig. S2(c). Note that $\tilde{\sigma}_7^z$ and $\tilde{\sigma}_1^z$ are corners of the plaquette Ising models at the red and blue sublattices, which are protected by the domain wall conservation when J dominates. In addition, \tilde{G}_r becomes the emergent symmetry under the high-frequency drive. These together give the long-lived corner modes \tilde{Z} and \tilde{X} .

THE MELTING OF HOSPT-PDTCs

The long-lived subharmonic responses of the two conjugate corner operators \tilde{Z} and \tilde{X} originate from the HOSPT phase of H_{eff} Eq. (S6). However, when any one of h_x , V_{xx} and V_{zz} is large enough, H_{eff} undergoes a quantum phase transition and the sub-harmonic response is no longer robust—the PDTC melts. In the previous section and the main text, we focused on the HOSPT-PDTC transition into an SSB-PDTC as $|V_{zz}|$ is increased. We now discuss the remaining perturbations.

Intuitively, when h_x is large, H_{eff} develops a paramagnetic ground state that close to a product state with all spin pointing towards $-\hat{x}$. In this case, both \tilde{Z} and \tilde{X} are destroyed and no time-crystalline order can be observed. In the dual picture, this corresponds to the destruction of the 2D plaquette Ising model by a large transverse field.

For the $V_{xx} \sum_{\langle ij \rangle} \sigma_i^x \sigma_j^x$ terms, when V_{xx} is large enough, H_{eff} develops a ferromagnetic ground state. However, since the symmetry that is spontaneously broken $G = G_r G_b$ is exactly the same as the π -pulse G , we can not observe any time-crystalline order because there is no sub-harmonic response—the system becomes dynamically trivial. We can also analyze the transition point in the dual picture, which is given by the transition point between a 2D Ising model with XX terms and a 2D plaquette Ising model with $ZZZZ$ terms.

To summarize these results, we construct the full phase diagram as a function of V_{zz} and V_{xx} [Fig. S3(a)]. In the green area with small V_{zz} and V_{xx} , the system is a HOSPT-PDTC where the time-crystalline order can be observed on \tilde{Z} and \tilde{X} . In the blue area with small V_{xx} but large V_{zz} , the system is an SSB-PDTC where the time-crystalline order can be observed at each $\tilde{\sigma}_i^z$ throughout the whole system. In the grey area with large V_{xx} , the system enters a dynamically trivial phase, where the underlying phase of H_{eff} is a ferromagnetic phase where G is spontaneously broken. By the self-duality, we know that the transition between HOSPT-PDTCs and SSB-PDTCs always occurs at $V_{zz} = 1$, which means the phase boundary f_3 is a vertical line below the three-phase intersection point O .

If $h_x = \epsilon = 0$, we can further use the duality to obtain a relation between f_1 and f_2 : We know that $(V_{zz}, f_2(V_{zz}))$ is the transition point between SSB-PDTC and the trivial phase under stabilizer strength $J = 1$, and $(V_{zz}, f_1(V_{zz}))$ is the transition

point between HOSPT-PDTC and trivial phase under plaquette Ising strength V_{zz} . Note that in the dual picture, the latter becomes the transition point $(1, f_1(V_{zz}))$ between SSB-PDTC and the trivial phase under stabilizer strength $\bar{J} = V_{zz}$. Therefore, we have

$$\frac{f_1(V_{zz})}{V_{zz}} = f_2\left(\frac{1}{V_{zz}}\right). \quad (\text{S22})$$

We can check that f_1 and f_2 indeed intersect at O since $f_1(1) = f_2(1)$. Also, we can calculate the position of the transition point A by

$$\lim_{V_{zz} \rightarrow 0} f_1(V_{zz}) = \lim_{V_{zz} \rightarrow \infty} \frac{f_2(V_{zz})}{V_{zz}}. \quad (\text{S23})$$

We numerically verify this phase diagram by calculating the order parameters $O_m = \prod_{i \in \text{red}, i \notin \text{corner}} K_i$ for HOSPT-PDTCs, $\langle \sigma_{c_1}^z \sigma_{c_2}^z \rangle$ for SSB-PDTCs, and $\langle \sigma_{c_1}^x \sigma_{c_2}^x \rangle$ for the dynamical trivial phase on a system with $M = N = 3$. The results are shown in Fig. S3(b-d), where we can clearly identify the phase boundaries f_1 , f_2 , and f_3 . Also note that $f_2(V_{zz})/V_{zz} \approx 0.625$ at $V_{zz} = 2$, which fits well with the transition point A occurring at $V_{xx} \approx 0.6$.

EXPERIMENTAL IMPLEMENTATIONS AND NUMERICAL SIMULATIONS

The superconducting transmon qubit arrays are a powerful platform for simulating quantum phases of matter [14, 15, 37, 39, 66, 77]. The HOSPT-PDTCs can be implemented on superconducting qubit arrays through a digital approach. To do this, we need to decompose the system dynamics $H_F(t)$ into sequences of experimentally implementable quantum gates. The circuit U_1 for the π -pulse can be readily identified as

$$U_1 = \prod_i R_{x,i}(\pi - \epsilon T). \quad (\text{S24})$$

For the dynamics generated by stabilizer operators $J \sum_{i \notin \text{corner}} K_i$, we first note that the dynamics of one stabilizer can be implemented as follows:

$$\begin{aligned} U_{K_k} &= \exp\left(-i J_k \Delta t \bigotimes_{\langle jk \rangle} Z_j \otimes X_k\right) \\ &= \cos(-J_k \Delta t) \bigotimes_{\langle jk \rangle} I_j \otimes I_k + i \sin(-J_k \Delta t) \bigotimes_{\langle jk \rangle} Z_j \otimes X_k \\ &= \sum_{q_j \in \{0,1\}} \left[\cos(-J_k \Delta t) \bigotimes_{\langle jk \rangle} |q_j\rangle \langle q_j| \otimes I_k + i \sin(-J_k \Delta t) \bigotimes_{\langle jk \rangle} (-1)^{q_j} |q_j\rangle \langle q_j| \otimes X_k \right] \\ &= \sum_{q_j \in \{0,1\}} \left[\bigotimes_{\langle jk \rangle} |q_j\rangle \langle q_j| \otimes Z_k^{\sum q_j} [\cos(-J_k \Delta t) I_k + i \sin(-J_k \Delta t) \otimes X_k] Z_k^{\sum q_j} \right] \\ &= \left[\prod_{\langle jk \rangle} \text{CZ}_{j,k} \right] R_{x,k}(2J_k \Delta t) \left[\prod_{\langle jk \rangle} \text{CZ}_{j,k} \right] \end{aligned} \quad (\text{S25})$$

where the stabilizer operator is applied at k and $\langle jk \rangle$ denotes the spins j that are neighbors of spin k . We note that all the two-qubit gates involved in this circuit are between nearest-neighboring qubits, which suit well the qubit connection geometry for existing programmable superconducting processors. By adjusting the rotation angle of the single qubit R_x gate, we effectively implement the evolution with arbitrary stabilizer strength and driving frequencies.

To implement $J \sum_{i \notin \text{corner}} K_i$, note that all stabilizer operators commute, we only need to place U_{K_k} together and arrange them with minimized circuit depth. This optimization involves first implementing stabilizer operators on qubits located on one sublattice, followed by implementation on another. The optimized circuit U_2 for a $M = 2, N = 3$ system is shown in Fig. S4(a). In this setup, qubits $q_1 \sim q_6$ reside on the blue sublattice, and qubits $q_7 \sim q_{12}$ reside on the red sublattice [labeled in Fig. S1(c)]. The dashed box represents a two-qubit gate block, where CZ gates can be executed on distinct sites simultaneously during experiments. The gates in the red (blue) box implement the stabilizers at qubits residing on the red (blue) sublattice. Except for

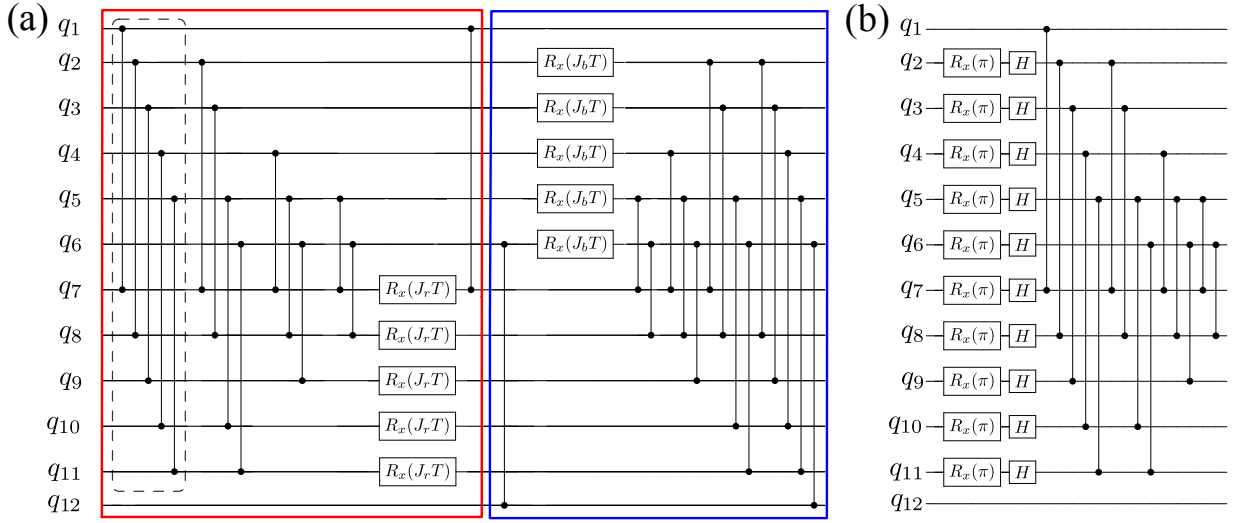


FIG. S4. The quantum circuits for (a) simulating the dynamics generated by stabilizer operators, and (b) preparing the system ground state of $J \sum_{i \notin \text{corner}} K_i$ with $M = 2, N = 3$. The qubit labels are the same as the ones shown in Fig. S1(c). All two-qubit CZ gates involve near-neighboring qubits.

those connected with corners, the CZ gates between red and blue boxes are mutually canceled. Notably, all two-qubit CZ gates are applied on adjacent qubits. It is worth emphasizing that this circuit is scalable, maintaining the same circuit depth regardless of the system size, thereby facilitating simulations for large systems on NISQ devices.

We note that the stabilizer operator at the blue corner JK_1 in $V(t)$ can also be implemented exactly by the method discussed above. Other perturbation terms in $V(t)$ are difficult to simulate exactly since, in general, they do not commute with $J \sum_{i \notin \text{corner}} K_i$. Nevertheless, note that the effect of perturbation terms is to break the integrability and break the $\mathbb{Z}_2 \times \mathbb{Z}_2$ symmetry of $J \sum_{i \notin \text{corner}} K_i$. This can also be done by adding other circuits after U_2 . For example, we can use the following circuits to approximate perturbations by single-body Pauli terms and two-body XX terms.

$$U_{\text{single}} = \prod_i R_{x,i}(h_x T) \prod_{i \in \text{red}} R_{y,i}(h_y T) \prod_{i \in \text{red}} R_{z,i}(h_z T), \quad (\text{S26})$$

$$U_{xx} = \prod_{k \in \text{blue}} \prod_{\langle jk \rangle} \text{CX}_{j,k} R_{x,k}(2V_{xx} \Delta t) \text{CX}_{j,k}. \quad (\text{S27})$$

Besides simulation of the system evolution, we also need to prepare the ground state $|\psi_g\rangle$ of $J \sum_{i \notin \text{corner}} K_i$ as the initial state to see the dynamics of HOSPT-PDTCs at zero temperature. To do this, we follow the idea in [78], where the authors use it to prepare the ground state of the toric code model. In our case, note that the ground state satisfies $\langle \psi_g | K_i | \psi_g \rangle = -1$ for all $i \notin \text{corners}$, we can write it as

$$|\psi_g\rangle \propto \prod_{i \notin \text{corners}} (I - K_i) |0\rangle^{\otimes N_{\text{qubits}}}. \quad (\text{S28})$$

To implement $I - K_i$, we can again use the scheme shown in Eq. (S25), which gives

$$\begin{aligned} I - K_i &= \bigotimes_{\langle ji \rangle} I \otimes I - \bigotimes_{\langle ji \rangle} Z \otimes X \\ &= \sum_{q_j \in \{0,1\}} \left[\bigotimes_{\langle ji \rangle} |q_j\rangle \langle q_j| \otimes I - (-1)^{\sum q_j} X \right] \\ &= \sum_{q_j \in \{0,1\}} \left[\bigotimes_{\langle ji \rangle} |q_j\rangle \langle q_j| \otimes Z^{\sum q_j} (I - X) Z^{\sum q_j} \right] \\ &= \left[\prod_{\langle ji \rangle} \text{CZ}_{j,i} \right] (I - X) \left[\prod_{\langle ji \rangle} \text{CZ}_{j,i} \right]. \end{aligned} \quad (\text{S29})$$

Since we start with $|0\rangle^{\otimes N_{\text{qubits}}}$, the ground state preparation can be further simplified as

$$\begin{aligned}
|\psi_g\rangle &\propto \prod_{\substack{i \in \text{red} \\ i \notin \text{corners}}} (I - K_i) \prod_{\substack{i \in \text{blue} \\ i \notin \text{corners}}} (I - K_i) |0\rangle^{\otimes N_{\text{qubits}}} \\
&\propto \prod_{\substack{i \in \text{red} \\ i \notin \text{corners}}} (I - K_i) |0\rangle_{\text{b,c}} \bigotimes_{\substack{i \in \text{blue} \\ i \notin \text{corners}}} |-\rangle \bigotimes_{i \in \text{red}} |0\rangle \\
&\propto \prod_{\substack{i \in \text{red} \\ i \notin \text{corners}}} \left[\prod_{\langle j,i \rangle} \text{CZ}_{j,i} \right] |0\rangle_{\text{b,c}} |0\rangle_{\text{r,c}} \bigotimes_{\substack{i \in \text{blue} \\ i \notin \text{corners}}} |-\rangle \bigotimes_{\substack{i \in \text{red} \\ i \notin \text{corners}}} |-\rangle \\
&\propto \prod_{\substack{i \in \text{red} \\ i \notin \text{corners}}} \left[\prod_{\langle j,i \rangle} \text{CZ}_{j,i} \right] \prod_{i \notin \text{corners}} H_i X_i |0\rangle^{\otimes N_{\text{qubits}}}.
\end{aligned} \tag{S30}$$

The circuit U_{gs} for preparing the ground state is shown in Fig. S4(b).

To show that time-crystalline orders of HOSPT-PDTCs can be observed on NISQ devices, we carry out numerical simulations with a realistic noise model. This is done with the help of the quantum virtual machine provided in the Cirq package in Python [76]. We run the virtual machine named ‘‘Weber,’’ which simulates running quantum circuits with noise data that mimic Google’s Sycamore processor. We first simulate the HOSPT-PDTCs at zero temperature, which is done by first applying U_{gs} and then repeatedly applying $U_F = U_{\text{single}} U_2 U_1$. We simulate different driving frequencies by changing T in U_2 and U_{single} . After each period, the magnetization at the blue corner is measured and gives $\langle \sigma_1^z(nT) \rangle = \langle U_{\text{gs}}^\dagger (U_F^\dagger)^n \sigma_1^z (U_F)^n U_{\text{gs}} \rangle$. The simulation results are shown in Fig. S5(a). We identify that the magnetization quickly decays to zero under low-frequency drive. In contrast, under high-frequency drive, the magnetization shows a long-lived subharmonic response. To verify that the quick decay in the low-frequency case is due to the thermalization of the system’s intrinsic dynamics but not the experimental noise, we also simulate the echo circuit $U_{\text{echo}} = U_{\text{gs}}^\dagger (U_F^\dagger)^n (U_F)^n U_{\text{gs}}$ and measure $\sqrt{\langle U_{\text{echo}}^\dagger \sigma_1^z U_{\text{echo}} \rangle}$. This value measures the effect of the experimental errors and noise [14]. By increasing the driving frequencies, the envelope of $\langle \sigma_1^z(nT) \rangle$ gradually saturates to the echo envelope. This indicates that under high-frequency drive, the system thermalizes very slowly by intrinsic dynamics, and the lifetime of the prethermal regime is extended.

At finite temperatures, the effectiveness of dimerization is also observed. Beginning with $|0\rangle^{\otimes N_{\text{qubits}}}$, we simulate different dimerization strength by changing J_r in U_2 . We repeatedly apply $U_F = U_{xx} U_2 U_1$ and measure the spin magnetization σ_1^z at the corner and σ_5^z in bulk. The simulation results are shown in Fig. S5(b-c). We can identify that with larger dimerization strength ($J_r = 5.31$), the lifetime of the subharmonic response at the corner is extended, while the one in bulk remains almost unchanged.

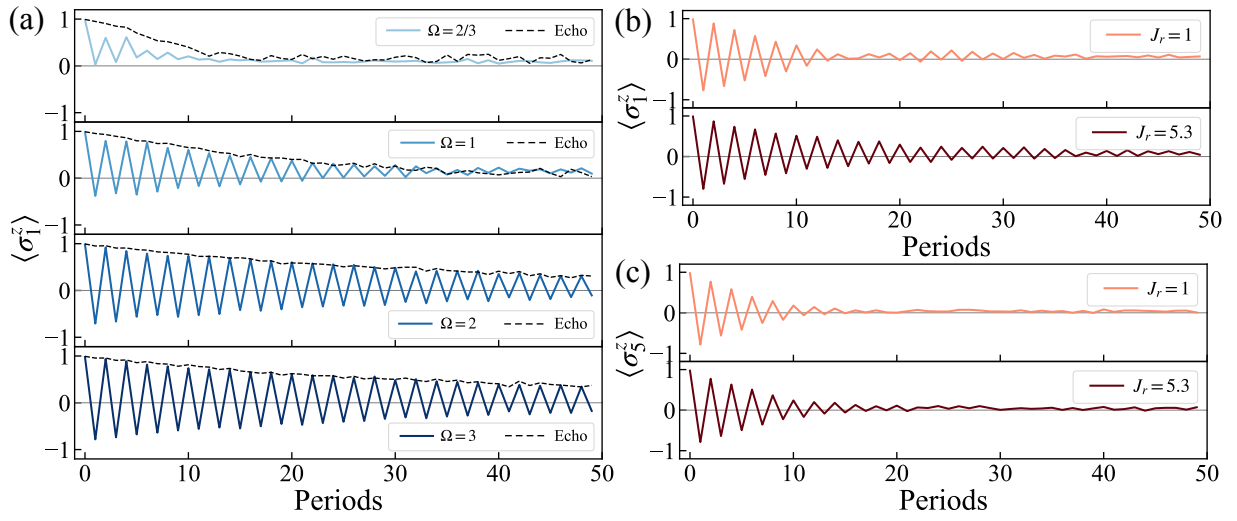


FIG. S5. Noisy simulations for dynamics of a HOSPT-PDTC. (a) The dynamics of corner spin magnetization at zero temperature. With increasing driving frequency, the dynamics show a long-lived subharmonic response with an envelope saturated with the echo dynamics envelope. (b-c) The dynamics of (b) corner spin magnetization and (c) bulk spin magnetization at finite temperatures. With increasing dimerization strength, only the corner spin lifetime of the subharmonic response is extended.